Review

Grain Boundary Wetting Phenomena in High Entropy Alloys Containing Nitrides, Carbides, Borides, Silicides, and Hydrogen: A Review

Boris Straumal [1,2,3,*], **Eugen Rabkin** [4], **Gabriel A. Lopez** [5], **Anna Korneva** [6], **Alexei Kuzmin** [7], **Alena Gornakova** [2], **Alexander Straumal** [2] and **Brigitte Baretzky** [1]

1   Institute of Nanotechnology, Karlsruhe Institute of Technology (KIT), 76344 Eggenstein-Leopoldshafen, Germany; brigitte.baretzky@kit.edu
2   Osipyan Institute of Solid State Physics, Russian Academy of Sciences, 142432 Chernogolovka, Russia; alenahas@issp.ac.ru (A.G.); a.str@issp.ac.ru (A.S.)
3   Chernogolovka Scientific Center, Russian Academy of Sciences, 142432 Chernogolovka, Russia
4   Department of Materials Science and Engineering, Technion-Israel Institute of Technology, Haifa 3200003, Israel; erabkin@tx.technion.ac.il
5   Physics Department, University of the Basque Country UPV/EHU, 48940 Leioa, Spain; gabrielalejandro.lopez@ehu.es
6   Institute of Metallurgy and Materials Science, Polish Academy of Sciences, 30-059 Cracow, Poland; a.korniewa@imim.pl
7   Institute of Solid State Physics, University of Latvia, LV-1063 Riga, Latvia; a.kuzmin@cfi.lu.lv
*   Correspondence: boris.straumal@kit.edu

Abstract: In this review, we analyze the structure of multicomponent alloys without principal components (they are also called high entropy alloys—HEAs), containing not only metals but also hydrogen, nitrogen, carbon, boron, or silicon. In particular, we discuss the phenomenon of grain boundary (GB) wetting by the melt or solid phase. The GB wetting can be complete or incomplete (partial). In the former case, the grains of the matrix are completely separated by the continuous layer of the second phase (solid or liquid). In the latter case of partial GB wetting, the second solid phase forms, between the matrix grains, a chain of (usually lenticular) precipitates or droplets with a non-zero value of the contact angle. To deal with the morphology of GBs, the new GB tie-lines are used, which can be constructed in the two- or multiphase areas of the multidimensional HEAs phase diagrams. The GBs in HEAs in the case of complete or partial wetting can also contain hydrides, nitrides, carbides, borides, or silicides. Thus, GB wetting by the hydrides, nitrides, carbides, borides, or silicides can be used in the so-called grain boundary chemical engineering in order to improve the properties of respective HEAs.

Keywords: high entropy alloys; grain boundary wetting; precipitation; phase transitions; phase diagrams

1. Introduction

The investigation of high-entropy alloys (HEAs) started in 2004 with the works of Cantor et al. and Yeh et al. [1,2]. Currently, several thousand papers have been devoted to HEAs. HEAs are frequently called alloys without principal components, or multiprincipal alloys. This is because they contain at least five different elements. The first HEAs were equimolar [1–4]. Their most attractive feature was that they always consisted of just one phase. It was the uniform solid solution with body-centered cubic (bcc) [5–7] or face-centered cubic (fcc) [8–11] lattice. However, it was later observed that this homogeneous solid solution is stable only in a certain range of compositions and at certain temperatures. Step by step, the interest in the inhomogeneous HEAs has gained momentum. This is because the presence of a second (third, etc.) phase can, for example, increase the strength of HEA and prevent the grain growth and the following softening at elevated temperature, etc. The elements of

heterogeneity can include the presence of other phases and the inhomogeneous distribution of elements in the bulk or in grain-boundaries (GBs), etc. The investigations of inhomogeneous HEAs are frequently called metastability engineering [12,13]. This review is devoted to the important type of inhomogeneity in HEAs, namely to the GB phase transformations. Such phase transitions include GB wetting with a liquid phase or a second solid phase and the appearance of different thin GB phases [14–17]. The GB wetting phenomena strongly depend on the temperature, pressure, and composition in a multicomponent system. They become especially interesting in HEAs including non-metallic elements such as nitrogen, carbon, boron, silicon, or hydrogen.

In this short review, we will consider the HEAs containing nitrides, carbides, borides, silicides, and hydrogen. We will present several important examples of complete and partial GB wetting by the melt and/or by the second solid phase. These examples do not exhaust all cases of GB wetting in HEAs. They are merely the most typical illustrations from recent publications. Indeed, similar microstructures can frequently be seen in papers devoted to HEAs.

2. Grain Boundary Wetting Phenomena

Usually, HEAs synthesis is based on the crystallization from the melt by induction or arc melting [5–11,18–35], plasma spark [36] or electric current assisted sintering [37,38], additive manufacturing by laser metal deposition [39], laser powder bed fusion [40,41] or laser or plasma cladding deposition of coatings [42–53], self-propagating high-temperature synthesis (SHS) [54], or brazing of dissimilar materials [55,56]. However, several HEA manufacturing technologies are based exclusively on the processes occurring in the solid state, such as solid-phase sintering [57] or sputter deposition of coatings [58]. In Figure 1, a schematic binary phase diagram is shown for the explanations of the GB wetting phenomena. When the hypo-eutectic liquid alloy (with concentration of component B below the eutectic point) begins to solidify, it first crosses the bulk liquidus line and enters into the two-phase L + α region of a phase diagram. Here, α is the solid phase (specifically a solid solution of component B in A) and L is the liquid phase. By a further decrease of the temperature, the bulk solidus line is crossed, the liquid phase L disappears, and only the solid solution, α, remains in the sample. However, if the solidification trajectory crosses the line of eutectic transformation instead of the solidus one, the rest of the melt transforms into the lamellar mixture of two solid solutions, namely α and β (see Figure 1). In the case of HEAs, the solidification process is much more complicated. For example, a 6D phase diagram is needed for the description of a six-component HEA. In such a case, between the single-phase melt, L, and the single-phase solid solution, α, areas, complicated regions with a number of solid and liquid phases can exist.

Consider now a polycrystalline sample in the L + α region of the phase diagram. This polycrystal contains GBs in the solid phase and interphase boundaries (IBs) between the solid and liquid phases. The triple junction between a GB and two IBs is characterized by a certain value of a contact angle, θ. Here, the two cases are possible. They are shown in insets (a) and (b) in Figure 1. In case (b) contact angle θ is non-zero, θ > 0. It is a partial (or incomplete) wetting of α/α GB by the melt, L. It takes place when the energy of the two solid/liquid IBs $2\sigma_{SL}$ is higher than the GB energy, σ_{GB}, $2\sigma_{SL} > \sigma_{GB}$, see scheme (b) in Figure 1. In the second case (a) of complete GB wetting, contact angle θ is zero, θ = 0. This is because the energy of two solid/liquid IBs is lower than the GB energy, $2\sigma_{SL} < \sigma_{GB}$. In this case, the α/α GB is replaced by a layer of the liquid phase L. As a result, the abutting grains are completely separated from each other by a rather thick liquid layer. In most cases, the contact angle, θ, between the GB and the melt decreases with increasing temperature [59–63] and reaches zero value at a certain temperature, T_w, known as the temperature of GB wetting transition. This is the transition from incomplete to complete GB wetting. Similar to bulk phase transformations, such GB phase transitions can be of first or second order [64–66]. In the former case, the derivative dθ/dT of the contact angle, θ, with respect to temperature, T, has a discontinuity at T_w [60,64,65]. It drops at T_w from

a certain finite value to zero. In the latter case of a second-order GB wetting transition (also called continuous), the $d\theta/dT$ derivative continuously decreases with increasing temperature. It becomes equal to zero at T_w without any sudden change [64,65].
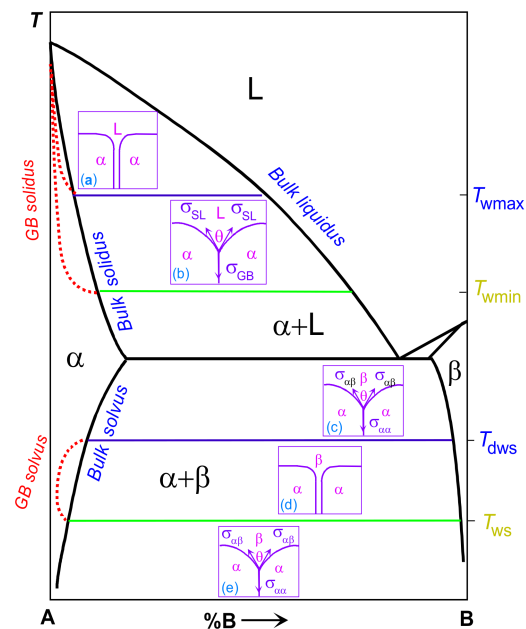

Figure 1. Schematic binary phase diagram for the explanation of GB wetting phenomena. Bold solid lines show the bulk phase transitions. Thin solid lines show the tie-lines for the wetting of GBs in the α-phase by the liquid phase at Twmin (green line) and Twmax (blue line) as well as by the second solid phase β at Tws (green line) and Tdws (blue line). The red dotted lines are the GB solidus (in the upper part of the scheme) and solvus lines (in the lower part of the scheme). Between the bulk and GB solidus lines, a GB contains a thin layer of the liquid-like phase, which is not stable in the bulk. Between the bulk and GB solvus lines, the α/α GB contains a thin layer of the β-like phase, which is not stable in the bulk. Insets show the schemes for the GB wetting: (a) complete wetting of α/α GB by the liquid phase L; (b) incomplete (partial) wetting of α/α GB by the liquid phase L; (c,e) incomplete (partial) wetting of α/α GB by the second solid phase β; (d) complete wetting of α/α GB by the second solid phase β. θ is the contact angle at the triple junction of a GB with two IBs. σGB is the energy of α/α GB. 2σSL is the energy of the two solid/liquid IBs. σαα is the energy of α/α GB. σββ is the energy of β/β GB. 2σαβ is the energy of the two α/β IBs.

The GB energy, σ_{GB}, strongly depends on the misorientation angle, ψ, and inclination angle, φ, of GBs [67]. GB misorientation angle, ψ, is the rotation angle around the crystallographic axis, which is common for both grains. Inclination angle, φ, measures the rotation of the GB plane from the symmetric position ($\varphi = 0$) when the misorientation, ψ, is fixed. It has deep minima at certain ψ and φ values [68]. These deep minima are sometimes observed at ψ values corresponding to the coincidence site lattices (CSL). For each CSL, the energy minima correspond to CSL planes densely packed with CSL nodes (and respective φ). For the non-CSL random GBs, the energy minima were associated with the high average interplanar spacing corresponding to the GB plane [69]. It is easy to see that the higher the σ_{GB}, the smaller the θ at the triple junction of a GB with two IBs [70]. The σ_{GB} spectrum in polycrystals is very broad [71]. This means that, at each temperature, a wide range of θ can be observed in a two-phase S + L polycrystal. Moreover, the contact angles, θ, for different GBs decrease at different rates at increasing temperatures. Because of this, the different GBs with different σ_{GB} should also possess the different T_w values. As a result, two GB wetting tie-lines appear in the phase diagram at T_{wmin} and T_{wmax}. The line at T_{wmin} marks the transition from incomplete to complete wetting for GBs having a maximum σ_{GB}. Below T_{wmin}, a polycrystal does not contain completely wetted GBs. Such polycrystal possesses

exclusively partially wetted GBs with $\theta > 0$. Above T_{wmin}, the polycrystal aquires the first completely wetted GBs. When temperature increases further, the number of completely wetted GBs also increases. The portion of completely wetted GBs reaches unity at T_{wmax}. T_{wmax} is shown in Figure 1 in the S + L area with a second tie-line. Above T_{wmax}, all GBs are completely wetted (see insets in the diagram). In such a structure, all grains are embedded in the melt and do not contact each other because it is thermodynamically unfavorable due to the $2\sigma_{\mathrm{SL}} < \sigma_{\mathrm{GB}}$. We see how the new tie-lines for GB wetting phase transition appear in the S + L two-phase region of a phase diagram. In the conventional phase diagrams, these tie-lines are not present because they do not consider the GBs in a system. Respectively, the microstructure of a solidified polycrystal should depend on the path along which the sample crosses the two-phase region during solidification.

Another interesting field in the schematic phase diagram in Figure 1 is the two-phase region where two solid phases, α and β, are in equilibrium. The α and β phases are two solid solutions, namely that of component B in component A (α-phase) and that of A in B (β-phase). Such $\alpha + \beta$ two-phase polycrystal contains three types of interfaces. First, these are the α/β IBs between the α and β phases, second, these are the α/α GBs in solid solution α, and third, these are the β/β GBs in solid solution β. These α/α GBs, β/β GBs, and α/β IBs can form four types of triple junctions (TJ). The first two types of TJs are the triple junctions of α/α GBs and TJs of β/β GBs. Another two types of TJs are α/α GBs with α/β TJs and β/β GBs with α/β IBs.

The possible relationships of the energies of these GBs $\sigma_{\alpha\alpha}$, $\sigma_{\beta\beta}$ and IBs $\sigma_{\alpha\beta}$ also allow the situations of complete and incomplete GB wetting. Thermodynamically, they are very similar to the GB wetting by the liquid phase (see above). Nevertheless, in the case of two solid phases, $\alpha + \beta$, the phase that wets the GB is also solid. Consider now the contact of α/α GB and two α/β IBs. We have to underline here that different α/β IBs have different energies, $\sigma_{\alpha\beta}$. The spectrum of $\sigma_{\alpha\beta}$ is at least as broad as that of $\sigma_{\alpha\alpha}$ or $\sigma_{\beta\beta}$. However, for simplicity we suppose here that these two α/β IBs have the same energy, $\sigma_{\alpha\beta}$. If the α/α GB energy, $\sigma_{\alpha\alpha}$, is less than the energy of two IBs $2\sigma_{\alpha\beta}$, $\sigma_{\alpha\alpha} < 2\sigma_{\alpha\beta}$, the wetting of the α/α GB by the second phase, β, is incomplete. In this case, the contact point of α/α GB and two α/β IBs is characterized by the nonzero contact angle $\theta > 0$ (see insets (c,e) in the lower part of Figure 1). If the condition $\sigma_{\alpha\alpha} > 2\sigma_{\alpha\beta}$ is fulfilled, then the contact angle will be equal to zero, $\theta = 0$. In turn, the α/α GB will be replaced by an interlayer of phase β. In this case, this is the complete wetting of α/α GB by the interlayer of a β-phase, as in inset (d) in Figure 1. The GB wetting transitions by the second solid phase have been directly observed in numerous binary metallic systems such as Ti–Fe [72,73], Ti–Co [74], Ti–Al–V [75], Zr–Nb [76], Al–Mg [77], Cu–Co [78], Al–Zn [79,80], Fe–Au [81], Cu–In [82,83] and Mg-RE alloys [84]. An example for the Al–Zn system is shown in Figure 2 (unpublished results from the work partially described in [82]). This Figure shows the light micrographs of the cross-sections of two Zn—5 wt.% Al samples annealed at 345 °C for 672 h (a) and at 275 °C for 2016 h (b). In Figure 2a, the (Zn)/(Zn) GB is completely wetted by the continuous layer of solid (Al) phase (appears dark). In Figure 2b, the solid (Al) phase forms the chain of lenticular particles with a certain contact angle, θ, along the (Zn)/(Zn) GB. It is, therefore, partially wetted.

In this consideration, we cannot see a qualitative difference between the situation of GB wetting by the liquid-phase and by the second solid-phase. On the other hand, the liquid phase has no crystal lattice and, therefore, contains no GBs. If the second phase, β, is solid, it has the GBs inside. As a result, the first solid phase, α, can also completely or partially wet the GBs in the second solid phase, β. If $\sigma_{\beta\beta} < 2\sigma_{\alpha\beta}$, the incomplete wetting of the β/β GB by the solid phase, α, takes place. If $\sigma_{\beta\beta} > 2\sigma_{\alpha\beta}$, then the β/β GB should be replaced by an interlayer of phase α, and the contact angle $\theta = 0$. This is the case for the complete wetting of the β/β GB by an interlayer of the α phase. Moreover, the conditions of complete wetting can be simultaneously fulfilled for β/β and α/α GBs, namely, $\sigma_{\beta\beta} > 2\sigma_{\alpha\beta}$ and $\sigma_{\beta\beta} > 2\sigma_{\alpha\beta}$. In this case, the GBs in a two-phase, $\alpha +$

β, polycrystal cannot exist at all, and only α/β IBs would remain. The two-dimensional section of this polycrystal will topologically resemble a chessboard.
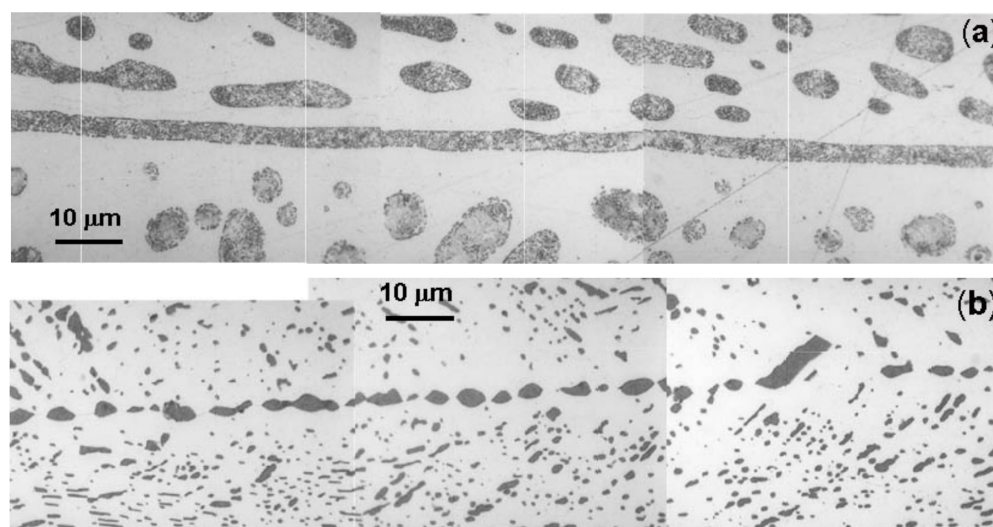

Figure 2. Optical micrographs of the cross-sections of Zn—5 wt.% Al samples annealed at (**a**) 345 °C for 672 h and (**b**) at 275 °C for 2016 h. Unpublished micrographs from our work done for [81]. The (Zn) phase appears bright and the (Al) phase appears dark. In Figure 2a, the (Zn)/(Zn) GB is completely wetted by the continuous layer of the solid (Al) phase. In Figure 2b, the (Zn)/(Zn) GB is incompletely wetted, and the solid (Al) phase forms the chain of lenticular particles with a certain contact angle, θ.

Moreover, in the case of GB wetting by the liquid phase, the σ_{GB} values usually decrease with increasing temperature more slowly in comparison with σ_{SL}. This is because the liquid phase has higher entropy in comparison with the solid one. As a result, the contact angle, θ, always decreases with increasing temperature and reaches zero θ = 0 at T_w. Above T_w, it remains equal to zero until the melting point. This behavior of the contact angle has been observed in numerous binary systems [60–62,64–66]. The temperature dependencies of $\sigma_{\alpha\alpha}$ and $\sigma_{\beta\beta}$ for GBs and IBs $\sigma_{\alpha\beta}$ have no obvious difference. Therefore, contact angle θ can both increase and decrease with increasing temperature. For example, the θ value in the Al–Mg alloys increases with increasing temperature, as in liquid phase GB wetting [77]. In the Al–Zn alloys, the θ value in TJs between (Al)/(Al) GBs and solid zinc decreased with decreasing temperature until it reached zero at the transition temperature, T_{ws}, from incomplete GB wetting the complete one [79]. Furthermore, the dependences $\sigma_{\alpha\alpha}$ (T) and $2\sigma_{\alpha\beta}$ (T) can intersect twice with changing temperature. In this case (inset (e) in Figure 1), the θ value can decrease with increasing temperature up to a certain temperature of the transition to the complete GB wetting, T_{ws}. Afterwards, all α/α GBs are wetted with interlayers of the second solid phase β (inset (d) in Figure 1). Further, a second transition occurs at T_{dws} when GB wetting disappears at the de-wetting temperature. Above T_{dws}, the α/α GBs are again incompletely wetted (inset (c) in Figure 1) by the second solid phase, β (as in, for example, the Cu–In alloys [82,83]).

In the schematic Figure 1, in the two-phase region, α + β, these tie-lines are shown for wetting at T_{ws} and for the de-wetting at T_{dws}. It is important to underline that this is a very simplified scheme. In fact, all GBs in a polycrystal have different energies, σ_{GB}, and for each value of σ_{GB} energy, there is its own value of the wetting phase transition temperature, T_w. This means that, in reality, the tie-lines at T_{ws} and T_{dws} should split into a spectrum of tie-lines, as in the case of GB wetting by the melt. Therefore, one has to draw not one tie-line for each temperature, T_{ws} and T_{dws}, but at least two lines for the maximum, T_{wsmax}, T_{dwsmax}, and minimum, T_{wsmin}, T_{dwsmin}, values of T_w. If we neglect again the energy, $\sigma_{\alpha\beta}$, difference between different IBs, one can expect that the α/α GBs with highest energy, $\sigma_{\alpha\alpha}$,

would become completely wetted at T_{wsmin} and completely de-wetted at T_{dwsmax}. In turn, the α/α GBs with the lowest energy, $\sigma_{\alpha\alpha}$, would become completely wetted at T_{wsmax} and completely de-wetted at T_{dwsmin}. In other words, the GBs with high energy, $\sigma_{\alpha\alpha}$, would remain wetted by the second solid phase in a broader temperature interval than the GBs with low energy.

We observed recently a comparable phenomenon for the wetting of GB TJs by the second solid phase [83,84]. Earlier, we studied the wetting of GB triple junctions by the liquid phase [85]. Namely, the GB TJs become completely wetted by the melt at a temperature, T_{wTJ}, lower than T_{wmin}. This follows from the simple geometric considerations. Thus, in the case of GB wetting, the GB with σ_{GB} is substituted by two IBs with $2\sigma_{\text{SL}}$. In the case of GB TJ, the "star" of three GBs is substituted by the triangle of IBs. In other words, we have a softer wetting condition, $\sigma_{\text{GB}} > 3^{1/2}\,\sigma_{\text{SL}}$, instead of $\sigma_{\text{GB}} > 2\sigma_{\text{SL}}$ and, therefore, T_{wTJ} should be lower than T_{wmin} [85,86]. In the case of TJ wetting by the second solid phase, not only T_{w} is present in the phase diagram but also T_{dw}. As a result, the GB TJs become wetted below T_{w} for GBs and will de-wet above T_{dw} for GBs. Thus, the temperature interval where GB TJs are wetted is broader than that for GBs.

Some indications of GB wetting by the second solid phase (such as the observed thick continuous GB layers) can also be found in numerous metallic HEAs such as $Al_{0.5}CoCuNiTi$ [9], $TiZrNbHfTa$ [87,88], $CrHfNbTaTi$ [10], $TiNbTaZrMo$ [89], $Mo_{0.5}VNbTiCr_x$ [27], $Co_{35}Cr_{32}Ni_{27}\text{-}Al_3Ti_3$ [17], $AlCoCrFeNiTi_{0.5}$ [90], $CoCrFeMnNi$ [36], $Co_{35}Cr_{25}Fe_{40-x}Ni_x$ [91], $TiNbTa_{0.5}ZrAl_{0.5}$ [92], and $CoNiAlWTaTi$ [93].

Another important point is that, in the case of GB wetting with the liquid phase, the equilibrium structure can be attained very quickly because of the high rate of mass transfer in the melt. One can count that the half-an-hour-long annealing is enough to reach thermodynamic equilibrium. If the phase that wets the GB is also solid, the mass transfer is significantly slower. This means that, by studying the GB wetting with the second solid phase, one has to employ very long annealing times to reach thermodynamic equilibrium, up to several months [77–79,82,83]. In the next sections, we discuss the works on HEAs where the published microstructures indicate the presence of the GB wetting phenomena. These four sections are devoted, respectively, to HEAs containing carbides and borides, silicides, hydrides, and nitrides.

3. GB Wetting Phenomena in HEAs Containing Carbides and Borides

The $MoNbRe_{0.5}TaW(TiC)_x$ HEA composite ingots were prepared by arc melting in a high-purity argon atmosphere [26]. They were composed of bcc solid solution and multi-component carbide (MC) with an fcc structure (see XRD patterns in Figure 3f). With increasing TiC addition, microstructure exhibits an evolution from hypo-eutectic (with x = 0.2, 0/5 and 0.8) to eutectic, and then to a hyper-eutectic one (with x = 1.0 and 1.5). This is explained by the analysis of the solidification process in the calculated equilibrium phase diagram [26]. Figure 3 shows scanning electron microscopy (SEM) images (a to e) and X-rays diffraction (XRD) patterns (f) of the $MoNbRe_{0.5}TaW(TiC)_x$ composites for x = 0.2 (a), x = 0.5 (b), x = 0.8 (c), x = 1.5 (d), and x = 1.0 (e). In hypo-eutectic samples, the liquid phase during solidification completely wets the GBs between the bcc matrix grains (see Figure 3a–c).

Further, this liquid phase decomposes according to the eutectic reaction into the bcc phase and MC. In hyper-eutectic samples (Figure 3d,e) the GB wetting is also quite well pronounced. Figure 4 shows the dark-field transmission electron microscopy (TEM) image of the $MoNbRe_{0.5}TaW(TiC)_{x1.0}$ composite (a) and corresponding element distribution maps for Mo, Nb, Re, Ta, W, Ti, and C. The high-magnification TEM micrograph (Figure 4a) shows that the eutectic mixture of bcc and multi-component carbide has a remarkable structure, similar to a chessboard (see above, the discussion of Figure 1 in Section 2). This could be the sign of mutual solid-state wetting of bcc/bcc and MC/MC GBs. In other words, the MC layers wet the bcc/bcc GBs and, simultaneously, the bcc layers wet the MC/MC GBs.
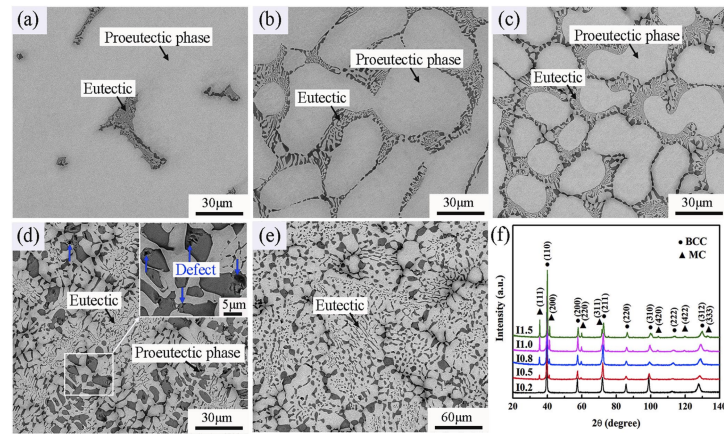
Figure 3. Back-scattered electron (BSE) SEM images (**a**–**e**) and XRD patterns (**f**) of the MoNbRe$_{0.5}$ TaW(TiC)$_x$ composites: (**a**) x = 0.2, (**b**) x = 0.5, (**c**) x = 0.8, (**d**) x = 1.5, (**e**) x = 1.0. Reprinted with permission from [26]. Copyright 2020 Elsevier.
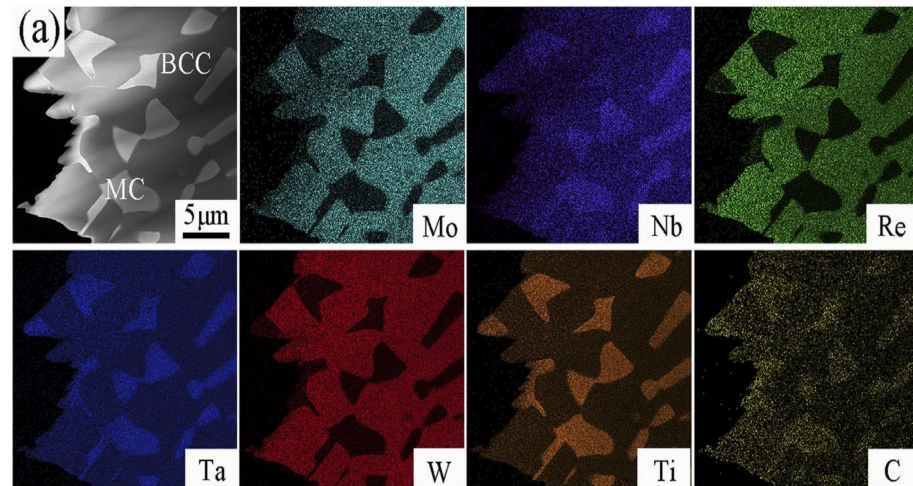

Figure 4. Dark-field TEM image of the MoNbRe$_{0.5}$TaW(TiC)$_{x1.0}$ composite (**a**) and corresponding element distribution maps (micrograhs Mo, Nb, Re, Ta, W, Ti, and C). Reprinted with permission from [26]. Copyright 2020 Elsevier.

The samples of CoCrFeNiMn–(Ti–Si–B(C)) HEAs were obtained by centrifugal met-allothermic self-propagating high-temperature synthesis (SHS) [53]. The SHS of highly exothermic mixtures proceeds at temperatures sufficient to obtain combustion products in the molten state (>2500 °C) and to prepare cast ingots. The idea of the work was to introduce the carbides and borides into a conventional matrix of CoCrFeNiM HEA with an fcc structure in order to improve its mechanical properties. Indeed, the microstructure of these HEAs was found to consist of an CoCrFeNiM HEA-based matrix and new structural inclusions of carbides and borides of titanium (see Figures 7–9 in [53]). They are concentrated in the Cr-rich bcc intergranular layers. These Cr-rich bcc phases with carbides and borides completely separate the fcc matrix grains. From our point of view, this is an indication of complete GB wetting in the fcc matrix by the liquid phase in solidification during SHS, or even GB wetting by the flat carbide and boride precipitates forming in solid-state during ingot cooling.

In [94], different Al$_{0.5}$CoCrFeNiTiC HEAs with small additions of Al, Ti, and C were prepared in a high-purity argon atmosphere by arc melting. The Al$_{0.5}$CoCrFeNiTiC HEAs consist of a bcc matrix and fcc metallic or carbide precipitates. Figure 5 demonstrates how the cast microstructures of all alloys studied in [94] depend on the chemical composition. In the left column in Figure 5 are low magnification back-scattered electron (BSE) micrographs

of reference alloy Al_{13} (a) and samples with $C_{0.25}$ (b), Al_{16}, (c), Ti_3 (d), and $Ti_3C_{0.25}$ (e). From each micrograph in the left column, a corresponding high magnification image is shown in the right column. It is well visible in Figure 5 how the carbide layers (Figure 5b,e) separate the grains of the bcc matrix, thus showing the wetting of bcc GBs by the melt during solidification. The GB wetting indications are also well visible in (Figure 5a,c,d).
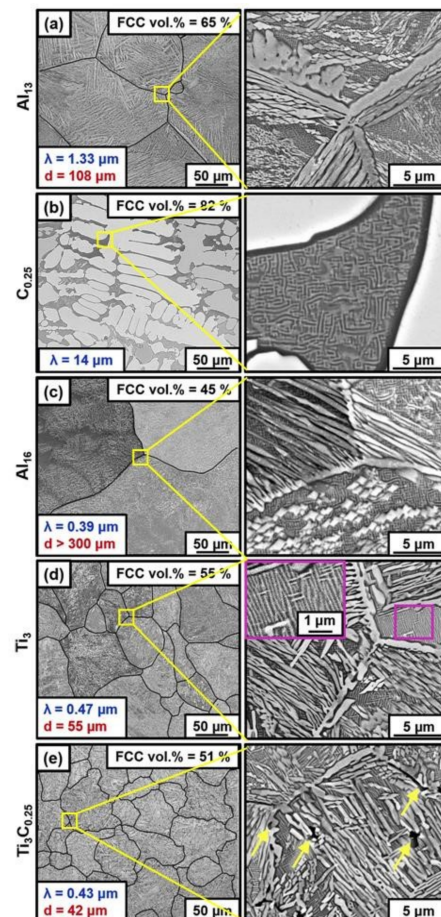

Figure 5. Effect of chemical composition on cast microstructures of all alloys studied in [94]. In the left column are low magnification BSE-micrographs of (**a**) reference Al_{13}, (**b**) $C_{0.25}$, (**c**) Al_{16}, (**d**) Ti_3, and (**e**) $Ti_3C_{0.25}$ alloys. From each micrograph in the left column, a corresponding high magnification image (marked in the left column by the yellow square) is shown in the right column. The volume fraction of the fcc phase, the prior grain size, d, as well as the mean thickness of the fcc plates, λ, are indicated at the top right and bottom left corners, respectively, of images (**a**–**e**). The pink framed inset in the right column of (**d**) shows the bcc/B2 interplate region, while the black dots highlighted with yellow arrows in the right column of (**e**) are TiC particles. Reprinted with permission from [94]. Copyright 2019 Elsevier.

The WC-(Al)CoCrCuFeNi cemented carbides with nominally high entropy alloy binders were studied in [95]. The conventional cemented carbides consist of WC grains surrounded by a cobalt-based binder [96–98]. It is well known that the cobalt-based binder wets the WC/WC GBs in cemented carbides during the liquid-phase sintering of these technologically important materials [96–98]. Approximately 10% of WC/WC GBs are completely wetted, and the other GBs are partially wetted with rather small contact angles. In [95], HEAs were manufactured using two different methods, namely mechanical alloying and gas atomization. The as-manufactured binder alloy powder after gas atomization was sieved, and its fine grain fraction was used for further experiments. The model cemented carbides (WC + HEA binder) were manufactured by the standard powder metallurgical

route in a planetary ball mill. Figure 6 shows the energy dispersive X-ray (EDX) mapping for Co, Cr, Cu, and O signals across the structure of CoCrCuFeNi sintered cemented carbide [95]. The HEA binder exhibits especially good contrast in the Cu map. The WC grains look black in the Cu map. They are clearly separated from each other by the Cu-rich HEA layers, appearing yellow. Approximately one-half of the WC/WC GBs are completely separated from each other by the HEA binder. The other half of WC/WC GBs are partially wetted by the HEA binder. The contact angles between the HEA binder and the WC/WC GBs in GB TJs are non-zero. Some flat lenticular binder particles (or droplets) are also visible between GB TJs in the WC/WC GBs.
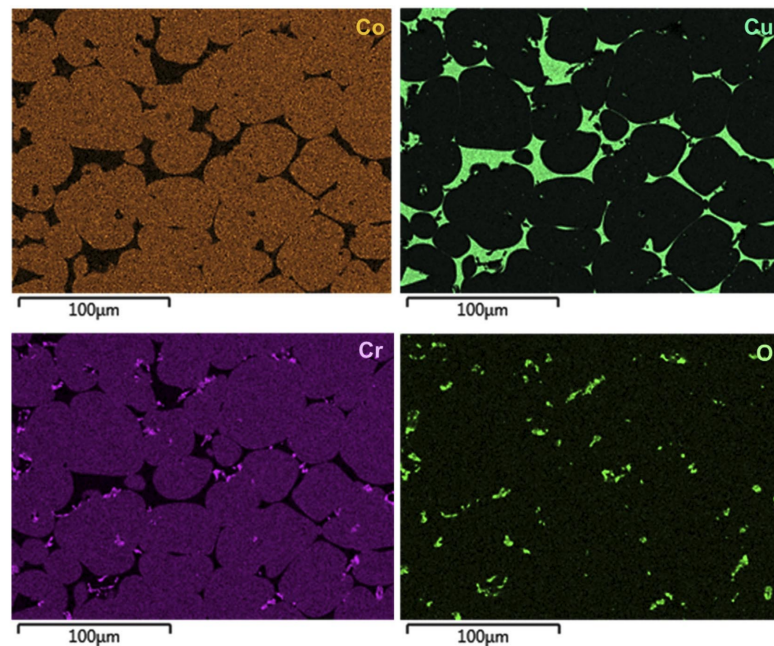
Figure 6. Co, Cr, Cu, and O signals of EDX mapping across the structure of CoCrCuFeNi sintered cemented carbide. Reprinted with permission from [95]. Copyright 2019 Elsevier.

4. GB Wetting Phenomena in HEAs Containing Silicides

Ingots with a nominal composition of FeCoNiCuTiSi$_x$ (x = 0, 0.05, 0.1, 0.2, 0.4, and 0.5) were prepared by arc-melting [31]. The as-cast samples contain the fcc matrix phase and minority C14 Laves phase, as well as bcc silicides. The portion of bcc silicides increased with increasing Si concentration, as did the lattice period of the bcc phase. It is well visible from micrographs published in [31] how the bcc phase surrounds the grains of the fcc matrix phase, thus wetting the fcc/fcc GBs. This is especially clear for x = 0.4 and 0.5.

In [19], one can find the indications for GB wetting by the liquid and by the second solid phase. The Nb–24Ti–18Si–5Al–5Cr–5Ge–5Sn–Si HEAs were prepared in the form of small buttons in a Ti-gettered Ar atmosphere using arc melting with a non-consumable tungsten electrode. The samples were annealed at 1400 °C for 100 h. For this purpose, the samples were wrapped in Ta foil and placed in an alumina crucible in a calibrated alumina tube furnace, where it was heat-treated under a constant flow of Ti-gettered Ar. Figure 7 shows the BSE images of the microstructure of the as-cast Nb–24Ti–18Si–5Al–5Cr–5Ge–5Sn–Si alloy for the bulk (a) and bottom (b) parts of the ingot. In the as-cast state, the matrix consists of an Nb_5Si_3 phase (Figure 7). Obviously, during the solidification, almost all Nb_5Si_3/Nb_5Si_3 GBs were completely wetted by the 10–20 μm thick layers of the melt. This melt transformed during the last stages of crystallization into an $Nb_3Sn + NbCr_2$ eutectic mixture. However, the conditions of solid-phase GB wetting are quite different in comparison to GB wetting by the melt. After heat treatment at 1400 °C for 100h, the microstructure strongly changed (see Figure 8). Figure 8 shows the BSE images of the microstructure of the Nb–24Ti–18Si–5Al–5Cr–5Ge–5Sn–Si alloy after heat treatment at

1400 °C for 100 h for the bulk (a) and bottom (b) parts of the ingot. Now the Nb_5Si_3 phase surrounds the Nb_3Sn and $NbCr_2$ grains. However, one can suppose that the Nb_3Sn conglomerates are polycrystalline and, therefore, not all Nb_3Sn/Nb_3Sn GBs are wetted by the Nb_5Si_3 phase.
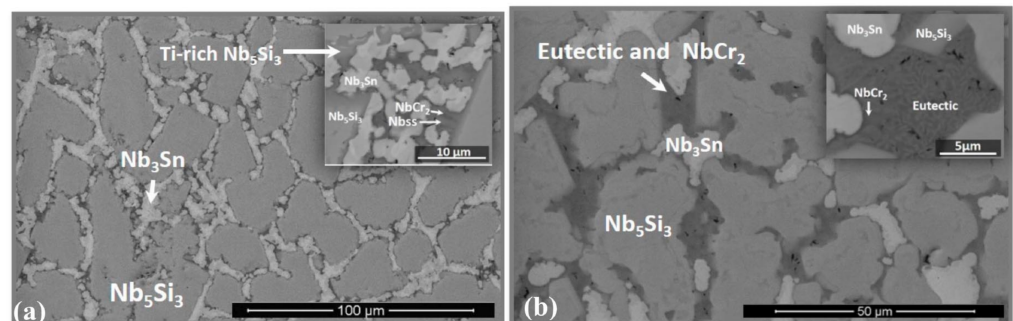

Figure 7. BSE images of the microstructure of the as-cast Nb–24Ti–18Si–5Al–5Cr–5Ge–5Sn–Si alloy. (**a**) bulk and (**b**) bottom. Reprinted with permission from [19].
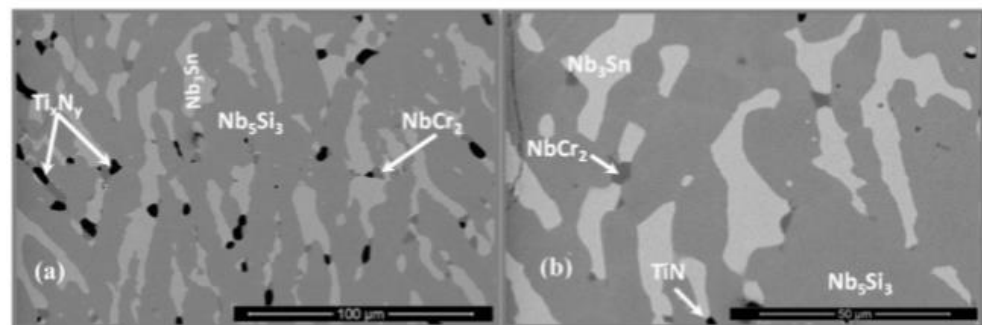

Figure 8. BSE images of the microstructure of the Nb-24Ti-18Si-5Al-5Cr-5Ge-5Sn-Si alloy after heat treatment at 1400 °C for 100 h. (**a**) bulk and (**b**) bottom. Reprinted with permission from [19].

5. GB Wetting Phenomena in HEAs Containing Hydrogen

The TiZrCrMnFeNi HEA was prepared from high-purity Ti (99.99%), Zr (99.5%), Cr (99.99%), Mn (99.95%), Fe (99.97%) and Ni (99.9%) elements by arc melting [28]. This HEA has a promising hydrogen storage performance. The mixture was rotated and re-melted six times to improve the compositional homogeneity. The as-cast state the alloy contained about 95 wt.% of C14 Laves phase (P63/mmc, $a = 0.493$ nm, $c = 0.809$ nm) and small amount of cubic phase (Pm-3m, $a = 0.305$ nm). It is one of the seldom HEAs not with fcc or bcc but with the hexagonal matrix. Figure 9 demonstrates the formation of coarse grains of hexagonal C14 Laves phase and fine grains of Ti- and Ni-rich cubic phase in this TiZrMnCrFeNi HEA. Figure 9a contains the orientation map obtained by the electron back-scattering diffraction (EBSD) with a beam step size of 1 μm. Figure 9b contains the EBSD phase map with a shorter beam step size of 300 nm. It is quite clear from the high-resolution EBSD map how the 3–5 μm thick layers of fcc phase (appearing blue in Figure 9b) separate about one-half of grains of the C14 Laves phase (they appear red in Figure 9b).

Figure 9c shows the SEM image and corresponding EDS elemental mappings for Ti, Zr, Cr, Mn, Fe and Ni. It can be seen from EDS elemental mappings for Ti- and Ni that the Ti- and Ni-rich fcc phase completely wets about one-half of the C14/C14 GBs (see Figure 9c). It is the indication of liquid phase GB wetting during solidification. For the examination of hydrogen storage performance, a disk sample with ~250 mg weight was crushed mildly in a glove box under an Ar atmosphere to reduce the particle size below 100 μm and loaded to a cell of a Sieverts-type gas absorption apparatus. The studied TiZrCrMnFeNi alloy absorbs and desorbs 1.7 wt.% of hydrogen. Unlike traditional

materials for room temperature hydrogen storage such as TiFe and Ti–V–Cr, the designated alloy does not need any activation process for hydrogen uptake. The alloy also has good resistance to the ambient atmosphere and can be handled and stored in the air, while many other hydrogen storage materials should be stored in an inert gas atmosphere to avoid the deactivation problem.
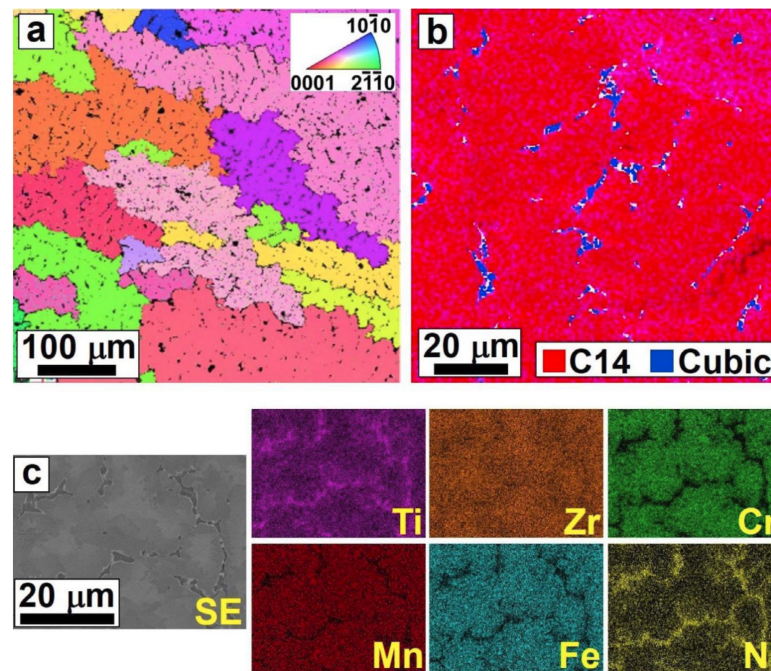

Figure 9. Formation of coarse grains of C14 Laves phase and fine grains of Ti- and Ni-rich cubic phase in high-entropy alloy TiZrMnCrFeNi. (**a**) EBSD orientation map with a beam step size of 1 μm, (**b**) EBSD phase map with a beam step size of 300 nm and (**c**) SEM image and corresponding EDS elemental mappings. Reprinted with permission from [28]. Copyright 2020 Elsevier.

The TiZrNbTa HEAs were prepared by using vacuum arc remelting followed by suction casting [30]. Disk samples were cut from the as-cast ingot and mechanically ground for hydrogen absorption. Hydrogen absorption and desorption were carried out in a self-made Sieverts device. The hydrogen absorption was conducted under a hydrogen pressure of 3×10^4 Pa at 800 °C for 10 min, and desorption was conducted under the vacuum of 0.1 Pa at 850 °C for 20 min. For comparison, the same heat treatment process (800 °C for 10 min and 800 °C for 10 min + 850 °C for 20 min) under vacuum was conducted on the as-cast TiZrNbTa sample. Figure 10 shows the XRD patterns (a) and (b–d) BSE images of as-received, hydrogen absorbed, and hydrogen desorbed TiZrNbTa samples. The microstructure of the as-cast sample consisted of a single bcc phase (see Figure 10a). However, it is visible in Figure 10b that the matrix bcc grains exhibiting bright contrast are surrounded by the layers appearing grey. It is the indication of the complete wetting of bcc/bcc GBs by the last portions of melt during solidification. During hydrogen absorption at 800 °C the initial bcc phase decomposed into two phases bcc1 and bcc2 (see Figure 10a,c). These phases remain in the alloy also after hydrogen desorption at 850 °C (see Figure 10a,d).

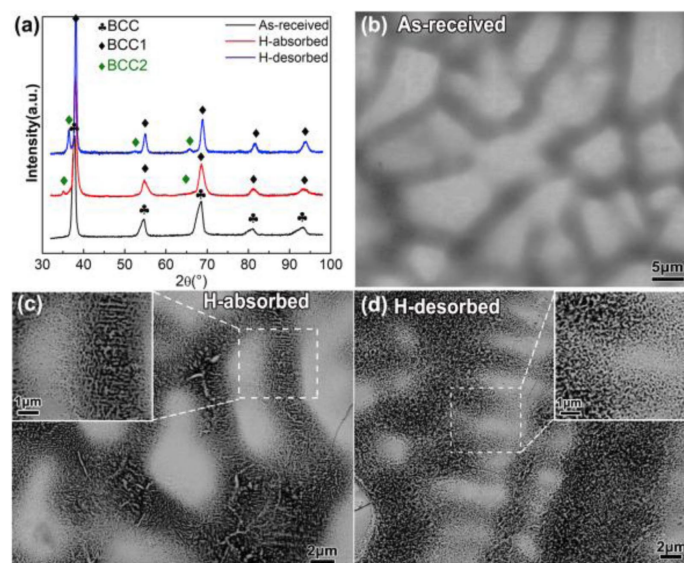**Figure 10.** (**a**) XRD patterns and (**b**–**d**) BSE images of as-received, hydrogen absorbed, and hydrogen desorbed TiZrNbTa samples. Reprinted with permission from [30]. Copyright 2020 Elsevier.

Figure 11 shows the bright-field TEM images and corresponding selected electron diffraction patterns of TiZrNbTa samples for as-received state (a), after hydrogen absorption (800 °C for 10 min) (b), after hydrogen desorption (800 °C for 10 min + 850 °C for 20 min) (c), and after similar heat-treatment (800 °C for 10 min + 850 °C for 20 min) but without hydrogen (d). These high magnification TEM micrographs show that after these heat treatments in the solid-state the fine-scale GB wetting takes place (see Figure 11b,c). Namely, the bcc1 and bcc1 phases form a structure similar to a chessboard (see above the discussion of Figure 1 in Section 2 or description of structure in Figure 4, Section 3). It can be the indication of mutual solid-state wetting of bcc1/bcc1 and bcc2/bcc2 GBs. In other words, bcc2 layers wet the bcc1/bcc1 GBs and, simultaneously, the bcc1 layers wet the bcc1/bcc1 GBs. It is remarkable, that after the same heat treatments but without hydrogen (Figure 11d) the formation of two phases bcc1 and bcc2 does not take place (and GB wetting transitions as well).
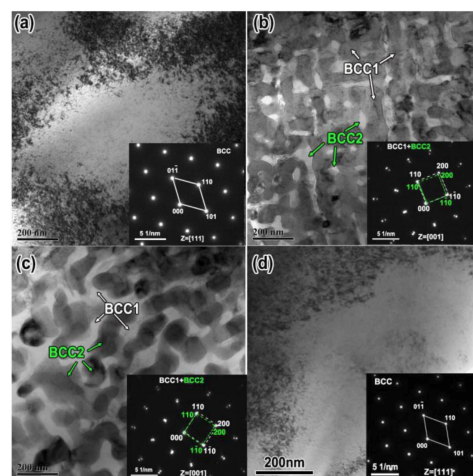

Figure 11. Bright-field images and corresponding selected electron diffraction patterns of TiZrNbTa samples. (**a**) As-received, (**b**) hydrogen absorbed (800 °C 10 min), (**c**) hydrogen desorbed (800 °C 10 min + 850 °C 20 min), and (**d**) heat-treated (800 °C 10 min + 850 °C 20 min) but without hydrogen. Reprinted with permission from [30]. Copyright 2020 Elsevier.

6. GB Wetting Phenomena in HEAs Containing Nitrides

Crystalline (Hf,Ta,Ti,V,Zr)N nitride thin films, with a high-entropy metal-sublattice, were synthesized at 440 °C by reactive magnetron sputtering using an equimolar Hf–Ta–Ti–V–Zr-compound target [58]. These coatings consisted of fcc mono-nitride. The atom probe tomography (APT) indicated the homogenous distribution of all elements in the fcc mono-nitride (Hf,Ta,Ti,V,Zr)N, even after annealing in vacuum at 1300 °C (see Figure 9a in [58]). However, after annealing at 1500 °C, a loss of nitrogen took place, and hexagonal nitride $(Ta,V)_2N$ formed. The very thin layers of this hexagonal $(Ta,V)_2N$ are located most probably in the GBs of mono-nitride (see Figure 9c in [58]). This can be an indication that, at 1500 °C, the sample is between the bulk solvus and the GB solvus (shown in Figure 1 by red dotted line) and contains thin layers of the GB phase. It has been observed earlier in binary and ternary systems that the few nm thin layers of GB phases can drastically increase the GB diffusivity [99], GB mobility [100], and GB sliding [101–105], etc.

Another two examples of GB wetting in HEAs by nitrides can be found in [105,106]. Cantor alloy FeCoCrNiMn (CA) and nitrogen-doped Cantor alloy (NCA) were both prepared by arc melting in a water-cooled copper mold [105]. Some of these NCA ingots were then aged at 800 °C in a muffle furnace for 24 h and then water quenched. CA and NCA ingots all had a single phase fcc structure. The NCA-aged alloy contained the chains of Cr_2N nitride precipitates in some fcc/fcc GBs. They witness the partial GB wetting by the nitride at 800 °C. In [106,107], the ingots with equiatomic composition $Fe_{20}Mn_{20}Cr_{20}Ni_{20}Co_{20}$ (HEA, at. %) as well as samples doped with 1 at. % nitrogen $Fe_{20}Mn_{20}Cr_{20}Ni_{20}Co_{19}N_1$ (HEA-1N) and with 1 at. % carbon $Fe_{20}Mn_{20}Cr_{20}Ni_{20}Co_{19}C_1$ (HEA-1C) were produced by vacuum induction melting and casting in a pure Ar atmosphere. The chains of nitrides (Figure 12a) and carbides (Figure 12b) were observed in GBs of the fcc matrix phase, demonstrating the partial GB wetting by nitride and carbide precipitates.
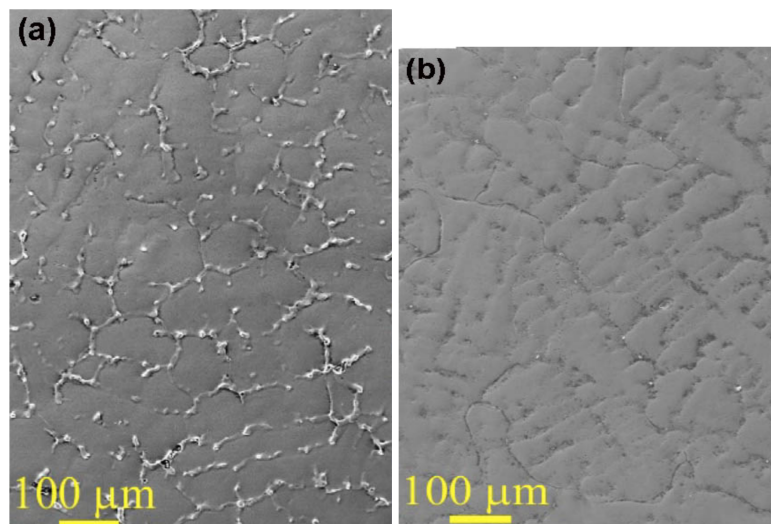

Figure 12. Typical BSE SEM images of $Fe_{20}Mn_{20}Cr_{20}Ni_{20}Co_{19}N_1$ (**a**) and $Fe_{20}Mn_{20}Cr_{20}Ni_{20}Co_{19}C_1$ (**b**) HEAs. The chains of nitrides (**a**) and carbides (**b**) are visible in GBs of the fcc matrix. Reprinted with permission from [107]. Copyright 2020 Elsevier.

7. Conclusions

In this paper, we provided several examples of GB wetting in HEAs containing hydrogen, nitrogen, carbon, boron, and silicon and, consequently, hydrides, nitrides, carbides, borides, and silicides. The given cases do not exhaust all possibilities of such GB wetting phenomena in HEAs. We mentioned only some typical ones from recent publications, and similar microstructures ca often be seen in other works on HEAs. Indeed, we can see now that modern HEAs can contain more than one multicomponent solid solution but also hydrides, nitrides, carbides, borides, and silicides. The shape and spatial

distribution of additional phases in these inhomogeneous HEAa can be determined by the GB wetting phenomena. Particularly, GB wetting can control the distribution of minor phases among the grains of the matrix phase. Previously, such phenomena have been extensively studied in binary metallic alloys [71–75,83,84,97,98,108]. These data can also be used for the description of multicomponent alloys. In particular, in the two- and multiphase areas of phase diagrams for HEAs, the additional tie-lines of the GB phase transitions can appear (see Figure 1). One can apply the new knowledge regarding GB wetting transformations in HEAs to modify their microstructure and properties.

The thick and thin GB layers of hydrides, nitrides, carbides, borides, and silicides can appear in HEAs during their manufacturing and/or subsequent annealing. The underlying phenomenon for the formation of such layers of GB phase(s) is the complete or incomplete GB wetting by the melt or another solid phase. Thus, the equilibrium layers of a second phase between matrix grains appear if the GB energy is higher than the energy of two interphase boundaries. The presence of these GB layers can have both positive and negative effect on the properties of HEAs. One can apply the GB wetting phenomena in hydride-, nitride-, carbide-, boride-, or silicide-containing HEAs to tailor their structure and properties. One can also use the knowledge on the tie-lines of GB wetting transitions as GB solidus and solvus lines in HEAs phase diagrams for the improvement of HEAs properties.

References

1.　Cantor, B.; Chang, I.T.H.; Knight, P.; Vincent, A.J.B. Microstructural development in equiatomic multicomponent alloys. *Mater. Sci. Eng. A* **2004**, *375–377*, 213–218. [CrossRef]

2.　Yeh, J.W.; Chen, S.K.; Lin, S.J.; Gan, J.Y.; Chin, T.S.; Shun, T.T.; Tsau, C.H.; Chang, S.Y. Nanostructured high-entropy alloys with multiple principal elements: Novel alloy design concepts and outcomes. *Adv. Eng. Mater.* **2004**, *6*, 299–303. [CrossRef]

3.　Senkov, O.N.; Wilks, G.B.; Miracle, D.B.; Chuang, C.P.; Liaw, P.K. Refractory high-entropy alloys. *Intermetallics* **2010**, *18*, 1758–1765. [CrossRef]

4.　Senkov, O.N.; Isheim, D.; Seidman, D.N.; Pilchak, A.L. Development of a refractory high entropy superalloy. *Entropy* **2016**, *18*, 102. [CrossRef]

5.　Yasuda, H.Y.; Yamada, Y.; Cho, K.; Nagase, T. Deformation behavior of HfNbTaTiZr high entropy alloy singe crystals and polycrystals. *Mater. Sci. Eng. A* **2021**, *809*, 140983. [CrossRef]

6.   Nagase, T.; Iijima, Y.; Matsugaki, A.; Ameyama, K.; Nakano, T. Design and fabrication of Ti–Zr-Hf-Cr-Mo and Ti–Zr-Hf-Co-Cr-Mo high entropy alloys as metallic biomaterials. *Mater. Sci. Eng. C* **2020**, *107*, 110322. [CrossRef] [PubMed]

7.   Eleti, R.R.; Chokshi, A.H.; Shibata, A.; Tsuji, N. Unique high-temperature deformation dominated by grain boundary sliding in heterogeneous necklace structure formed by dynamic recrystallization in HfNbTaTiZr BCC refractory high entropy alloy. *Acta Mater.* **2020**, *183*, 64–77. [CrossRef]

8.   Yao, H.; Liu, Y.; Sun, X.; Lu, Y.; Wang, T.; Li, T. Microstructure and mechanical properties of $Ti_3V_2NbAl_xNi_y$ low-density refractory multielement alloys. *Intermetallics* **2021**, *133*, 107187. [CrossRef]

9.   Yi, J.; Wang, L.; Tang, S.; Yang, L.; Xu, M.; Liu, L. Microstructure and mechanical properties of $Al_{0.5}CoCuNiTi$ high entropy alloy. *Phil. Mag.* **2021**, *101*, 1176–1187. [CrossRef]

10.   Yi, J.; Tang, S.; Zhang, C.; Xu, M.; Yang, L.; Wang, L.; Zeng, L. Microstructure and mechanical properties of a new refractory equiatomic CrHfNbTaTi high-entropy alloy. *JOM* **2021**, *73*, 934–940. [CrossRef]

11.   Nong, Z.; Wang, H.; Wang, D.; Zhu, J. Investigation on structural stability of as-cast $Al_{0.5}CrCuFeMnTi$ high entropy alloy. *Vacuum* **2020**, *182*, 109686. [CrossRef]

12.   Jung, Y.; Lee, K.; Hong, S.J.; Lee, J.K.; Han, J.; Kim, K.B.; Liaw, P.K.; Lee, C.; Song, G. Investigation of phase-transformation path in TiZrHf(VNbTa)x refractory high-entropy alloys and its effect on mechanical property. *J. Alloys Compd.* **2021**, *886*, 161187. [CrossRef]

13.   Sun, F.; Zhang, J.Y.; Marteleur, M.; Brozek, C.; Rauch, E.F.; Veron, M.; Vermaut, P.; Jacques, P.J.; Prima, F. A new titanium alloy with a combination of high strength, high strain hardening and improved ductility. *Scr. Mater.* **2015**, *94*, 17–20. [CrossRef]

14.   Chang, L.-S.; Straumal, B.; Rabkin, E.; Gust, W.; Sommer, F. The solidus line of the Cu–Bi phase diagram. *J. Phase Equil.* **1997**, *18*, 128–135. [CrossRef]

15.   Chang, L.-S.; Rabkin, E.; Straumal, B.; Lejcek, P.; Hofmann, S.; Gust, W. Temperature dependence of the grain boundary segregation of Bi in Cu polycrystals. *Scr. Mater.* **1997**, *37*, 729–735. [CrossRef]

16.   Chang, L.-S.; Rabkin, E.; Straumal, B.; Hoffmann, S.; Baretzky, B.; Gust, W. Grain boundary segregation in the Cu–Bi system. *Defect Diff. Forum* **1998**, *156*, 135–146. [CrossRef]

17.   Schölhammer, J.; Baretzky, B.; Gust, W.; Mittemeijer, E.; Straumal, B. Grain boundary grooving as an indicator of grain boundary phase transformations. *Interf. Sci.* **2001**, *9*, 43–53. [CrossRef]

18.   Du, X.H.; Huo, X.F.; Chang, H.T.; Li, W.P.; Duan, G.S.; Huang, J.C.; Wu, B.L.; Zou, N.F.; Zhang, L. Superior strength-ductility combination of a Co-rich CoCrNiAlTi high entropy alloy at room and cryogenic temperatures. *Mater. Res. Express* **2020**, *7*, 034001. [CrossRef]

19.   Hernández-Negrete, O.; Tsakiropoulos, P. On the microstructure and isothermal oxidation at 800 and 1200 °C of the Nb–24Ti–18Si–5Al–5Cr–5Ge–5Sn (at. %) silicide-dased alloy. *Materials* **2020**, *13*, 722. [CrossRef] [PubMed]

20.   Yi, J.; Wang, L.; Xu, M.; Yang, L. Two new 3d transition metals AlCrCuFeTi and AlCrCuFeV high-entropy alloys: Phase components, microstructures, and compressive properties. *Appl. Phys. A* **2021**, *127*, 74. [CrossRef]

21.   Mukarram, M.; Mujahid, M.; Yaqoob, K. Design and development of CoCrFeNiTa eutectic high entropy alloys. *J. Mater. Res. Technol.* **2021**, *10*, 1243–1249. [CrossRef]

22.   Guo, Z.; Liu, R.; Wang, C.T.; He, Y.; He, Y.; Ma, Y.; Hu, X. Compressive Mechanical properties and shock-induced reaction behavior of a Ti–29Nb–13Ta–4.6Zr alloy. *Met. Mater. Int.* **2020**, *26*, 1498–1505. [CrossRef]

23.   Jia, Y.; Zhang, L.; Li, P.; Ma, X.; Xu, L.; Wu, S.; Jia, Y.; Wang, G. Microstructure and mechanical properties of Nb–Ti–V–Zr refractory medium-entropy alloys. *Front. Mater.* **2020**, *7*, 172. [CrossRef]

24.   Petroglou, D.; Poulia, A.; Mathiou, C.; Georgatis, E.; Karantzalis, A.E. A further examination of MoTaxNbVTi (x = 0.25, 0.50, 0.75 and 1.00 at. %) high-entropy alloy system: Microstructure, mechanical behavior and surface degradation phenomena. *Appl. Phys. A* **2020**, *126*, 364. [CrossRef]

25.   Zhao, J.; Utton, C.; Tsakiropoulos, P. On the microstructure and properties of Nb-12Ti-18Si-6Ta-2.5W-1Hf (at. %) silicide-based alloys with Ge and Sn additions. *Materials* **2020**, *13*, 1778. [CrossRef]

26.   Wei, Q.; Luo, G.; Zhang, J.; Jiang, S.; Chen, P.; Shen, Q.; Zhang, L. Designing high entropy alloy-ceramic eutectic composites of $MoNbRe_{0.5}TaW(TiC)_x$ with high compressive strength. *J. Alloys Compd.* **2020**, *818*, 152846. [CrossRef]

27.   Xiang, C.; Fu, H.M.; Zhang, Z.M.; Han, E.-H.; Zhang, H.F.; Wang, J.Q.; Hu, G.D. Effect of Cr content on microstructure and properties of $Mo_{0.5}VNbTiCr_x$ high-entropy alloys. *J. Alloys Compd.* **2020**, *818*, 153352. [CrossRef]

28.   Edalati, P.; Floriano, R.; Mohammadi, A.; Li, Y.; Zepon, G.; Li, H.-W.; Edalati, K. Reversible room temperature hydrogen storage in high-entropy alloy TiZrCrMnFeNi. *Scr. Mater.* **2020**, *178*, 387–390. [CrossRef]

29.   Xiao, D.H.; Zhou, P.F.; Wu, W.Q.; Diao, H.Y.; Gao, M.C.; Song, M.; Liaw, P.K. Microstructure, mechanical and corrosion behaviors of AlCoCuFeNi-(Cr,Ti) high entropy alloys. *Mater. Des.* **2017**, *116*, 438–447. [CrossRef]

30.   Zhang, C.; Wu, Y.; You, L.; Qiu, W.; Zhang, Y.; Yuan, Y.; Lu, Z.; Song, X. Nanoscale phase separation of TiZrNbTa high entropy alloy induced by hydrogen absorption. *Scr. Mater.* **2020**, *178*, 503–507. [CrossRef]

31.   Qu, H.Z.; Gong, M.L.; Liu, F.F.; Gao, B.Y.; Bai, J.; Gao, Q.Z.; Li, S. Microstructure, mechanical properties and magnetic properties of $FeCoNiCuTiSi_x$ high-entropy alloys. *Sci. China Technol. Sci.* **2020**, *63*, 459–466. [CrossRef]

32.   Erdogani, A.; Gök, M.S.; Zeytin, S. Analysis of the high-temperature dry sliding behavior of $CoCrFeNiTi_{0.5}Al_x$ high-entropy alloys. *Friction* **2020**, *8*, 198–207. [CrossRef]

33. Barron, P.J.; Carruthers, A.W.; Fellowes, J.W.; Jones, N.G.; Dawson, H.; Pickering, E.J. Towards V-based high-entropy alloys for nuclear fusion applications. *Scr. Mater.* **2020**, *176*, 12–16. [CrossRef]

34. Kosorukova, T.A.; Gerstein, G.; Odnosum, V.V.; Koval, Y.N.; Maier, H.J.; Firstov, G.S. Microstructure formation in cast TiZrHf-CoNiCu and CoNiCuAlGaIn high entropy shape memory alloys: A comparison. *Materials* **2019**, *12*, 4227. [CrossRef]

35. Gurel, S.; Yagci, M.B.; Canadinc, D.; Gerstein, G.; Bal, B.; Maier, H.J. Fracture behavior of novel biomedical Ti-based high entropy alloys under impact loading. *Mater. Sci. Eng. A* **2021**, *803*, 140456. [CrossRef]

36. Eißmann, N.; Mühle, U.; Gaitzsch, U.; Walther, G.; Weißgärber, T.; Kieback, B. Precipitation hardening of high entropy alloy CoCrFeMnNi containing titanium. *J. Alloys Compd.* **2021**, *857*, 157610. [CrossRef]

37. Döleker, K.M.; Erdogan, A.; Zeytin, S. Laser re-melting influence on isothermal oxidation behavior of electric current assisted sintered CoCrFeNi, CoCrFeNiAl$_{0.5}$ and CoCrFeNiTi$_{0.5}$Al$_{0.5}$ high entropy alloys. *Surf. Coat. Technol.* **2021**, *407*, 126775. [CrossRef]

38. Erdogan, A.; Döleker, K.M.; Zeytin, S. Effect of laser re-melting on electric current assistive sintered CoCrFeNiAl$_x$Ti$_y$ high entropy alloys: Formation, micro-hardness and wear behaviors. *Surf. Coat. Technol.* **2020**, *399*, 126179. [CrossRef]

39. Cui, W.; Li, W.; Chen, W.-T.; Liou, F. Laser Metal Deposition of an AlCoCrFeNiTi$_{0.5}$ High-entropy alloy coating on a Ti6Al4V substrate: Microstructure and oxidation behavior. *Crystals* **2020**, *10*, 638. [CrossRef]

40. Huber, F.; Bartels, D.; Schmidt, M. In-situ alloy formation of a WMoTaNbV refractory metal high entropy alloy by laser powder bed fusion (PBF-LB/M). *Materials* **2021**, *14*, 3095. [CrossRef]

41. Dada, M.; Popoola, P.; Mathe, N.; Pityana, S.; Adeosun, S.; Aramide, O.; Lengopeng, T. Process optimization of high entropy alloys by laser additive manufacturing. *Eng. Rep.* **2020**, *2*, 12252. [CrossRef]

42. Zeng, X.; Liu, Z.; Wu, G.; Tong, X.; Xiong, Y.; Cheng, X.; Wang, X.; Yamaguchi, T. Microstructure and high-temperature properties of laser cladded AlCoCrFeNiTi$_{0.5}$ high-entropy coating on Ti 6Al-4V alloy. *Surf. Coat. Technol.* **2021**, *418*, 127243. [CrossRef]

43. Gu, Z.; Mao, P.; Gou, Y.; Chao, Y.; Xi, S. Microstructure and properties of MgMoNbFeTi$_2$Y$_x$ high entropy alloy coatings by laser cladding. *Surf. Coat. Technol.* **2020**, *402*, 126303. [CrossRef]

44. Gu, Z.; Xi, S.; Mao, P.; Wang, C. Microstructure and wear behavior of mechanically alloyed powder Al$_x$Mo$_{0.5}$NbFeTiMn$_2$ high entropy alloy coating formed by laser cladding. *Surf. Coat. Technol.* **2020**, *401*, 126244. [CrossRef]

45. Zhang, Y.; Han, T.; Xiao, M.; Shen, Y. Tribological behavior of diamond reinforced FeNiCoCrTi$_{0.5}$ carbonized highentropy alloy coating. *Surf. Coat. Technol.* **2020**, *401*, 126233. [CrossRef]

46. Xiang, K.; Chen, L.-Y.; Chai, L.; Guo, N.; Wang, H. Microstructural characteristics and properties of CoCrFeNiNb$_x$ high-entropy alloy coatings on pure titanium substrate by pulsed laser cladding. *Appl. Surf. Sci.* **2020**, *517*, 146214. [CrossRef]

47. Zhang, Y.; Han, T.; Xiao, M.; Shen, Y. Microstructure and properties of laser-clad FeNiCoCrTi$_{0.5}$Nb$_{0.5}$ high-entropy alloy coating. *Mater. Sci. Technol.* **2020**, *36*, 811–818. [CrossRef]

48. Wang, X.; Liu, Q.; Huang, Y.; Xie, L.; Xu, Q.; Zhao, T. Effect of Ti content on the microstructure and corrosion resistance of CoCrFeNiTi$_x$ high entropy alloys prepared by laser cladding. *Materials* **2020**, *13*, 2209. [CrossRef]

49. Li, Y.; Liang, H.; Nie, Q.; Qi, Z.; Deng, D.; Jiang, H.; Cao, Z. Microstructures and wear resistance of CoCrFeNi$_2$V$_{0.5}$Ti$_x$ high-entropy alloy coatings prepared by laser cladding. *Crystals* **2020**, *10*, 352. [CrossRef]

50. Gu, Z.; Xi, S.; Sun, C. Microstructure and properties of laser cladding and CoCr$_{2.5}$FeNi$_2$Ti$_x$ high-entropy alloy composite coatings. *J. Alloys Compd.* **2020**, *819*, 152986. [CrossRef]

51. Xu, Y.; Li, Z.; Liu, J.; Chen, Y.; Zhang, F.; Wu, L.; Hao, J.; Liu, L. Microstructure evolution and properties of laser cladding CoCrFeNiTiAl$_x$ high-entropy alloy coatings. *Coatings* **2020**, *10*, 373. [CrossRef]

52. Wang, J.; Zhang, B.; Yu, Y.; Zhang, Z.; Zhu, S.; Wang, Z. Ti content effect on microstructure and mechanical properties of plasma-cladded CoCrFeMnNiTi$_x$ high-entropy alloy coatings. *Surf. Topogr. Metrol. Prop.* **2020**, *8*, 015004. [CrossRef]

53. Sanin, V.N.; Ikornikov, D.M.; Golosov, O.A.; Andreev, D.E.; Yukhvid, V.I. Centrifugal metallothermic SHS of cast Co–Cr–Fe–Ni–Mn–(X) alloys. *Russ. J. Non-Ferr. Met.* **2020**, *61*, 436–445. [CrossRef]

54. Li, Y.; Shi, Y. Phase assemblage and properties of laser cladded Ti$_x$CrFeCoNiCu high-entropy alloy coating on aluminum. *Mater. Res. Express* **2020**, *7*, 036519. [CrossRef]

55. Wang, G.; Sheng, G.; Yu, Q.; Yuan, X.; Sun, J.; Jiao, Y.; Zhang, Y. Investigation of intergranular penetration behavior in CrMnFeCoNi HEA/304 SS dissimilar brazing joints. *Intermetallics* **2020**, *126*, 106940. [CrossRef]

56. Wang, G.; Sheng, G.; Sun, J.; Wei, Y.; Gao, X.; Yu, Z.; Yuan, X. Mechanical properties and microstructure evolution of CrMnFeCoNi HEA/304 SS dissimilar brazing joints. *J. Alloys Compd.* **2020**, *829*, 154520. [CrossRef]

57. Shkodich, N.; Sedegov, A.; Kuskov, K.; Busurin, S.; Scheck, Y.; Vadchenko, S.; Moskovskikh, D. Refractory high-entropy HfTaTiNbZr-based slloys by combined use of ball milling and spark plasma sintering: Effect of milling intensity. *Metals* **2020**, *10*, 1268. [CrossRef]

58. Kirnbauer, A.; Kretschmer, A.; Koller, C.M.; Wojcik, T.; Panet, V.; Hans, M.; Schneider, J.M.; Polcik, P.; Mayrhofer, P.H. Mechanical properties and thermal stability of reactively sputtered multiprincipal-metal Hf–Ta–Ti–V–Zr nitrides. *Surf. Coat. Technol.* **2020**, *389*, 125674. [CrossRef]

59. Straumal, B.; Molodov, D.; Gust, W. Tie lines of the grain boundary wetting phase transition in the Al–Sn system. *J. Phase Equilibria* **1994**, *15*, 386–391. [CrossRef]

60. Straumal, B.; Gust, W.; Molodov, D. Wetting transition on the grain boundaries in Al contacting with Sn-rich melt. *Interface Sci.* **1995**, *3*, 127–132. [CrossRef]

61. Straumal, B.; Gust, W.; Watanabe, T. Tie lines of the grain boundary wetting phase transition in the Zn-rich part of the Zn–Sn phase diagram. *Mater. Sci. Forum* **1999**, *294–296*, 411–414. [CrossRef]

62. Straumal, A.B.; Yardley, V.A.; Straumal, B.; Rodin, A.O. Influence of the grain boundary character on the temperature of transition to complete wetting in Cu–In system. *J. Mater. Sci.* **2015**, *50*, 4762–4771. [CrossRef]

63. Kogtenkova, O.A.; Straumal, A.B.; Afonikova, N.S.; Mazilkin, A.A.; Kolesnikova, K.I.; Straumal, B. Grain boundary wetting phase transitions in peritectic copper—Cobalt alloys. *Phys. Sol. State* **2016**, *58*, 743–747. [CrossRef]

64. Straumal, B.; Gornakova, A.S.; Kogtenkova, O.A.; Protasova, S.G.; Sursaeva, V.G.; Baretzky, B. Continuous and discontinuous grain boundary wetting in the Zn–Al system. *Phys. Rev. B* **2008**, *78*, 054202. [CrossRef]

65. Gornakova, A.S.; Straumal, B.; Tsurekawa, S.; Chang, L.-S.; Nekrasov, A.N. Grain boundary wetting phase transformations in the Zn–Sn and Zn–In systems. *Rev. Adv. Mater. Sci.* **2009**, *21*, 18–26.

66. Straumal, B.; Muschik, T.; Gust, W.; Predel, B. The wetting transition in high and low energy grain boundaries in the Cu(In) system. *Acta Met. Mater.* **1992**, *40*, 939–945. [CrossRef]

67. Maksimova, E.L.; Shvindlerman, L.S.; Straumal, B. Transformation of Σ17 special tilt boundaries to general boundaries in tin. *Acta Met.* **1988**, *36*, 1573–1583. [CrossRef]

68. Ernst, F.; Finnis, M.W.; Koch, A.; Schmidt, C.; Straumal, B.; Gust, W. Structure and energy of twin boundaries in copper. *Z. Metallk.* **1996**, *87*, 911–922.

69. Sutton, A.P.; Balluffi, R.W. Overview 61. On geometric criteria for low interfacial energy. *Acta Met.* **1987**, *35*, 2177–2201. [CrossRef]

70. Straumal, B.; Baretzky, B. Grain boundary phase transitions and their influence on properties of polycrystals. *Interf. Sci.* **2004**, *12*, 147–155. [CrossRef]

71. Straumal, B.; Shvindlerman, L.S. Regions of existence of special and non-special grain boundaries. *Acta Met.* **1985**, *33*, 1735–1749. [CrossRef]

72. Straumal, B.; Kilmametov, A.R.; Ivanisenko, Y.; Gornakova, A.S.; Mazilkin, A.A.; Kriegel, M.J.; Fabrichnaya, O.B.; Baretzky, B.; Hahn, H. Phase transformations in Ti-Fe alloys induced by high pressure torsion. *Adv. Eng. Mater.* **2015**, *17*, 1835–1841. [CrossRef]

73. Gornakova, A.S.; Straumal, B.; Nekrasov, A.N.; Kilmametov, A.; Afonikova, N.S. Grain boundary wetting by a second solid phase in Ti–Fe alloys. *J. Mater. Eng. Perform.* **2018**, *27*, 4989–4992. [CrossRef]

74. Gornakova, A.S.; Prokofiev, S.I.; Straumal, B.; Kolesnikova, K.I. Growth of (αTi) grain boundary layers in Ti–Co alloys. *Russ. J. Non-Ferr. Met.* **2016**, *57*, 703–709. [CrossRef]

75. Gornakova, A.S.; Straumal, B.; Prokofiev, S.I. Coarsening of (αTi)+(βTi) microstructure in the Ti–Al–V alloy at constant temperature. *Adv. Eng. Mater.* **2018**, *20*, 1800510. [CrossRef]

76. Straumal, B.; Gornakova, A.S.; Kucheev, Y.O.; Baretzky, B.; Nekrasov, A.N. Grain boundary wetting by a second solid phase in the Zr–Nb alloys. *J. Mater. Eng. Perform.* **2012**, *21*, 721–724. [CrossRef]

77. Straumal, B.; Baretzky, B.; Kogtenkova, O.A.; Straumal, A.B.; Sidorenko, A.S. Wetting of grain boundaries in Al by the solid Al_3Mg_2 phase. *J. Mater. Sci.* **2010**, *45*, 2057–2061. [CrossRef]

78. Straumal, B.; Kogtenkova, O.A.; Straumal, A.B.; Kuchyeyev, Y.O.; Baretzky, B. Contact angles by the solid-phase grain boundary wetting in the Co–Cu system. *J. Mater. Sci.* **2010**, *45*, 4271–4275. [CrossRef]

79. Protasova, S.G.; Kogtenkova, O.A.; Straumal, B.; Zięba, P.; Baretzky, B. Inversed solid-phase grain boundary wetting in the Al–Zn system. *J. Mater. Sci.* **2011**, *46*, 4349–4353. [CrossRef]

80. López, G.A.; Mittemeijer, E.J.; Straumal, B. Grain boundary wetting by a solid phase microstructural development in a Zn–5 wt. % Al alloy. *Acta Mater.* **2004**, *52*, 4537–4545. [CrossRef]

81. Amram, D.; Amouyal, Y.; Rabkin, E. Encapsulation by segregation—A multifaceted approach to gold segregation in iron particles on sapphire. *Acta Mater.* **2016**, *102*, 342–351. [CrossRef]

82. Straumal, B.; Kogtenkova, O.A.; Kolesnikova, K.I.; Straumal, A.B.; Bulatov, M.F.; Nekrasov, A.N. Reversible "wetting" of grain boundaries by the second solid phase in the Cu–In system. *JETP Lett.* **2014**, *100*, 535–539. [CrossRef]

83. Straumal, B.; Kogtenkova, O.; Bulatov, M.; Nekrasov, A.; Baranchikov, A.; Baretzky, B.; Straumal, A. Wetting of grain boundary triple junctions by intermetallic Delta-phase in the Cu–In alloys. *J. Mater. Sci.* **2021**, *58*, 7840–7848. [CrossRef]

84. Straumal, A.; Mazilkin, I.; Tzoy, K.; Straumal, B.; Bryła, K.; Baranchikov, A.; Eggeler, G. Bulk and surface low temperature phase transitions in the Mg-alloy EZ33A. *Metals* **2020**, *10*, 1127. [CrossRef]

85. Straumal, B.; Kogtenkova, O.; Zięba, P. Wetting transition of grain boundary triple junctions. *Acta Mater.* **2008**, *56*, 925–933. [CrossRef]

86. Straumal, A.B.; Mazilkin, I.A.; Tsoi, K.V.; Baretzky, B.; Straumal, B. "Wetting" phase transitions by the second solid phase for linear defects (grain boundary triple junctions). *JETP Lett.* **2020**, *112*, 257–261. [CrossRef]

87. Dobbelstein, H.; George, E.P.; Gurevich, E.L.; Kostka, A.; Ostendorf, A.; Laplanche, G. Laser metal deposition of refractory high-entropy alloys for high-throughput synthesis and structure-property characterization. *Int. J. Extrem. Manuf.* **2021**, *3*, 015201. [CrossRef]

88. Yang, C.; Aoyagi, K.; Bian, H.; Chiba, A. Microstructure evolution and mechanical property of a precipitation-strengthened refractory high-entropy alloy HfNbTaTiZr. *Mater. Lett.* **2019**, *254*, 46–49. [CrossRef]

89. Navi, A.S.; Haghighi, S.E.; Haghpanahi, M.; Momeni, A. Investigation of microstructure and corrosion of TiNbTaZrMo high-entropy alloy in the simulated body fluid. *J. Bionic. Eng.* **2021**, *18*, 118–127. [CrossRef]

90. Kong, D.; Guo, J.; Liu, R.; Zhang, X.; Song, Y.; Li, Z.; Guo, F.; Xing, X.; Xu, Y.; Wang, W. Effect of remelting and annealing on the wear resistance of AlCoCrFeNiTi$_{0.5}$ high entropy alloys. *Intermetallics* **2019**, *114*, 106560. [CrossRef]

91. Bai, X.; Fang, W.; Chang, R.; Yu, H.; Zhang, X.; Yin, F. Effects of Al and Ti additions on precipitation behavior and mechanical properties of Co$_{35}$Cr$_{25}$Fe$_{40-x}$Ni$_x$ TRIP high entropy alloys. *Mater. Sci. Eng. A* **2019**, *767*, 138403. [CrossRef]

92. Cao, Y.; Liu, Y.; Li, Y.; Liu, B.; Fu, A.; Nie, Y. Precipitation behavior and mechanical properties of a hot-worked TiNbTa0.5ZrAl$_{0.5}$ refractory high entropy alloy. *Int. J. Refract. Met. Hard Mater.* **2020**, *86*, 105132. [CrossRef]

93. Li, W.; Li, L.; Antonov, S.; Feng, Q. Effective design of a Co–Ni–Al–W–Ta–Ti alloy with high γ′ solvus temperature andmicrostructural stability using combined CALPHAD and experimental approaches. *Mater. Des.* **2019**, *180*, 107912. [CrossRef]

94. Asabre, A.; Kostka, A.; Stryzhyboroda, O.; Pfetzing-Micklich, J.; Hecht, U.; Laplanche, G. Effect of Al, Ti and C additions on Widmanstätten microstructures and mechanical properties of cast Al$_{0.6}$CoCrFeNi compositionally complex alloys. *Mater. Des.* **2019**, *184*, 108201. [CrossRef]

95. Mueller-Grunz, A.; Alveen, P.; Rassbach, S.; Useldinger, R.; Moseley, S. The manufacture and characterization of WC-(Al)CoCrCuFeNi cemented carbides with nominally high entropy alloy binders. *Int. J. Refr. Met. Hard Mater.* **2019**, *84*, 105032. [CrossRef]

96. Konyashin, I.; Lachmann, F.; Ries, B.; Mazilkin, A.A.; Straumal, B.; Kübel, C.; Llanes, L.; Baretzky, B. Strengthening zones in the Co matrix of WC–Co cemented carbides. *Scr. Mater.* **2014**, *83*, 17–20. [CrossRef]

97. Straumal, B.; Konyashin, I.; Ries, B.; Straumal, A.B.; Mazilkin, A.A.; Kolesnikova, K.I.; Gusak, A.M.; Baretzky, B. Pseudopartial wetting of WC/WC grain boundaries in cemented carbides. *Mater. Lett.* **2015**, *147*, 105–108. [CrossRef]

98. Konyashin, I.; Straumal, B.; Ries, B.; Bulatov, M.F.; Kolesnikova, K.I. Contact angles of WC/WC grain boundaries with binder in cemented carbides with various carbon content. *Mater. Lett.* **2017**, *196*, 1–3. [CrossRef]

99. Straumal, B.; Noskovich, O.I.; Semenov, V.N.; Shvindlerman, L.S.; Gust, W.; Predel, B. Premelting transition on 38° <100> tilt grain boundaries in (Fe–10at. %Si)–Zn alloys. *Acta Met. Mater.* **1992**, *40*, 795–801. [CrossRef]

100. Molodov, D.A.; Czubayko, U.; Gottstein, G.; Shvindlerman, L.S.; Straumal, B.; Gust, W. Acceleration of grain boundary motion in Al by small additions of Ga. *Phil. Mag. Lett.* **1995**, *72*, 361–368. [CrossRef]

101. Mabuchi, M.; Higashi, K.; Langdon, T. An investigation of the role of a liquid phase in Al–Cu–Mg metal matrix composites exhibiting high strain rate superplasticity. *Acta Met. Mater.* **1992**, *42*, 1739–1745. [CrossRef]

102. Mabuchi, M.; Imai, T.; Kubo, K.; Higashi, K.; Tanimura, S. Superplastic-like behavior in Al–Mg–Si composites reinforced with α-Si$_3$N$_4$ or β- Si$_3$N$_4$ whiskers. *Mater. Lett.* **1991**, *12*, 276–280. [CrossRef]

103. Mabuchi, M.; Imai, T.; Kubo, K.; Higashi, K.; Tanimura, S. Superplastic properties in a Si$_3$N$_4$ Si$_3$N$_{4w}$/Al–Zn–Mg composite extruded at a reduction ratio of 100:1. *Mater. Lett.* **1991**, *12*, 330–334. [CrossRef]

104. Koike, J.; Mabuchi, M.; Higashi, K. In situ observation of partial melting in superplastic aluminum alloy composites at high temperatures. *Acta Met. Mater.* **1995**, *43*, 199–206. [CrossRef]

105. Mabuchi, M.; Higashi, K.; Okada, Y.; Tanimura, S.; Imai, T.; Kubo, K. Very high strain-rate superplasticity in a particulate Si$_3$N$_4$ 6061 aluminum composite. *Scr. Met. Mater.* **1991**, *25*, 2517–2522. [CrossRef]

106. Chung, K.S.; Yiu, P.M.; Hung, T.F.; Shek, C.H. Strengthening and deformation mechanism of a Fe$_{20}$Co$_{20}$Cr$_{20}$Mn$_{20}$Ni$_{20}$ high entropy alloy with high nitrogen content. *J. Alloys Compd.* **2021**, *871*, 159587. [CrossRef]

107. Astafurova, E.G.; Reunova, K.A.; Melnikov, E.V.; Panchenko, M.Y.; Astafurov, S.V.; Maier, G.G.; Moskvina, V.A. On the difference in carbon- and nitrogen-alloying of equiatomic FeMnCrNiCo high-entropy alloy. *Mater. Lett.* **2020**, *276*, 128183. [CrossRef]

108. Mazilkin, A.; Straumal, B.; Protasova, S.G.; Gorji, S.; Straumal, A.B.; Katter, M.; Schütz, G.; Barezky, B. Grain boundary oxide layers in NdFeB-based permanent magnets. *Mater. Des.* **2021**, *199*, 109417. [CrossRef]